

Distribution characteristics of inclusions along with the surface sliver defect on the exposed panel of automobile: A quantitative electrolysis method

Xiao-qian Pan, Jian Yang, Joohyun Park, and Hideki Ono

Cite this article as:

Xiao-qian Pan, Jian Yang, Joohyun Park, and Hideki Ono, Distribution characteristics of inclusions along with the surface sliver defect on the exposed panel of automobile: A quantitative electrolysis method, *Int. J. Miner. Metall. Mater.*, 27(2020), No. 11, pp. 1489-1498. <https://doi.org/10.1007/s12613-020-1973-8>

View the article online at [SpringerLink](#) or [IJMMM Webpage](#).

Articles you may be interested in

Peng Fei, Yi Min, Cheng-jun Liu, and Mao-fa Jiang, [Effect of continuous casting speed on mold surface flow and the related near-surface distribution of non-metallic inclusions](#), *Int. J. Miner. Metall. Mater.*, 26(2019), No. 2, pp. 186-193. <https://doi.org/10.1007/s12613-019-1723-y>

Min-nan Feng, Yu-cong Wang, Hao Wang, Guo-quan Liu, and Wei-hua Xue, [Reconstruction of three-dimensional grain structure in polycrystalline iron via an interactive segmentation method](#), *Int. J. Miner. Metall. Mater.*, 24(2017), No. 3, pp. 257-263. <https://doi.org/10.1007/s12613-017-1403-8>

Huan-yu Zhang, Rui Li, Wen-wu Liu, Mei Zhang, and Min Guo, [Research progress in lead-less or lead-free three-dimensional perovskite absorber materials for solar cells](#), *Int. J. Miner. Metall. Mater.*, 26(2019), No. 4, pp. 387-403. <https://doi.org/10.1007/s12613-019-1748-2>

Rui Wang, Yan-ping Bao, Zhi-jie Yan, Da-zhao Li, and Yan Kang, [Comparison between the surface defects caused by Al₂O₃ and TiN inclusions in interstitial-free steel auto sheets](#), *Int. J. Miner. Metall. Mater.*, 26(2019), No. 2, pp. 178-185. <https://doi.org/10.1007/s12613-019-1722-z>

Liang Yang and Guo-guang Cheng, [Characteristics of Al₂O₃, MnS, and TiN inclusions in the remelting process of bearing steel](#), *Int. J. Miner. Metall. Mater.*, 24(2017), No. 8, pp. 869-875. <https://doi.org/10.1007/s12613-017-1472-8>

Jing Guo, Xing-run Chen, Shao-wei Han, Yan Yan, and Han-jie Guo, [Evolution of plasticized MnO–Al₂O₃–SiO₂-based nonmetallic inclusion in 18wt%Cr8wt%Ni stainless steel and its properties during soaking process](#), *Int. J. Miner. Metall. Mater.*, 27(2020), No. 3, pp. 328-339. <https://doi.org/10.1007/s12613-019-1945-z>



IJMMM WeChat



QQ author group

Distribution characteristics of inclusions along with the surface sliver defect on the exposed panel of automobile: A quantitative electrolysis method

Xiao-qian Pan¹⁾, Jian Yang¹⁾, Joohyun Park²⁾, and Hideki Ono³⁾

1) State Key Laboratory of Advanced Special Steel, School of Materials Science and Engineering, Shanghai University, Shanghai 200444, China

2) Department of Materials Engineering, Hanyang University, Ansan 426-791, South Korea

3) Faculty of Sustainable Design, University of Toyama, Toyama-ken 930-8555, Japan

(Received: 28 September 2019; revised: 22 December 2019; accepted: 26 December 2019)

Abstract: The specific distribution characteristics of inclusions along with the sliver defect were analyzed in detail to explain the formation mechanism of the sliver defect on the automobile exposed panel surface. A quantitative electrolysis method was used to compare and evaluate the three-dimensional morphology, size, composition, quantity, and distribution of inclusions in the defect and non-defect zone of automobile exposed panel. The Al_2O_3 inclusions were observed to be aggregated or chain-like shape along with the sliver defect of about 3–10 μm . The aggregation sections of the Al_2O_3 inclusions are distributed discretely along the rolling direction, with a spacing of 3–7 mm, a length of 6–7 mm, and a width of about 3 mm. The inclusion area part is 0.04%–0.16% with an average value of 0.08%, the inclusion number density is 40 mm^{-2} and the inclusion average spacing is 25.13 μm . The inclusion spacing is approximately 40–160 μm , with an average value of 68.76 μm in chain-like inclusion parts. The average area fraction and number density of inclusions in the non-defect region were reduced to about 0.002% and 1–2 mm^{-2} , respectively, with the inclusion spacing of 400 μm and the size of Al_2O_3 being 1–3 μm .

Keywords: automobile exposed panel; sliver defect; quantitative electrolysis; three-dimensional inclusions; aggregated inclusions; chain-like inclusions

1. Introduction

The alloyed hot-dip galvanized sheets for automobile exposed panels with high surface quality are under urgent development with the increasing demands by high-grade automobile users. More attention has been given to controlling the surface defects caused by steelmaking, which are further interwoven with the defects formed in hot rolling, cold rolling, and hot-dip galvanizing processes. Therefore, it is difficult to identify, estimate, and develop the defects caused by steelmaking.

There have been many studies on the surface linear defects caused by steelmaking for the exposed automobile panel, which can be divided into three categories by source: inclusions [1], mold powder [2], and bubbles [3–4]. Al_2O_3 , SiO_2 , $\text{MgO}\cdot x\text{CaO}$ inclusions, and mold powders are found along with these linear defects, that are usually entrapped by the evolution of mold powder or captured by the near-meniscus hook in the mold's primary solidified shell to degrade the surface quality of the car exposed panel [5–12]. Yu *et al.* [12] believed that large subcutaneous inclusions, mainly from

deoxidized materials and trapped mold powders, could result in surface defects, similar to the results obtained by Das *et al.* [13]. Cui *et al.* [14] reported that Al_2O_3 , SiO_2 , and silicon aluminum from the slag entry under the surface defects are the main reasons for the formation of defects during cold rolling. Genzano *et al.* [15] concluded that only direct observation of the defect with SEM (scanning electron microscope) couldn't clearly identify the origin of the defect. Although numerous surface defect studies have been conducted, they are mainly focused on qualitative analysis [16–18], and only a few of them investigate quantitatively to obtain an in-depth understanding of the distribution characteristics of inclusions, and mold powders along with the linear defects on a cold-rolled automobile exposed panel board.

Besides, to study the distribution characteristics of inclusions along with the linear defect, the precise three-dimensional analysis of inclusions is of great importance. Electrolysis approaches are often used to analyze the three-dimensional inclusion morphology [19–25] that can be classified into electrolyte-based methods: acidic and neutral. The high efficiency of electrolysis can be achieved with acid electro-

Corresponding author: Jian Yang E-mail: yang_jian@t.shu.edu.cn

© University of Science and Technology Beijing and Springer-Verlag GmbH Germany, part of Springer Nature 2020

lyte, but it can destroy the inclusions of oxide, sulfide, and nitride. The minimal unstable non-metallic inclusions in steel can be extracted without causing damage by using a neutral electrolyte, but the process's by-products are complex. Also, the current density and efficiency are reportedly low. The electrolysis method has been rarely used so far to detect inclusions in surface defects.

The purpose of this study is to show the specific distribution characteristics of inclusions on cold-rolled alloyed hot-dip galvanized sheet in the defect and non-defect zone for the automobile exposed panel to explain the sliver defect formation mechanism. Quantitative electrolysis methods were used to compare and quantitatively evaluate the three-dimensional morphology, size, composition, quantity, and distribution of inclusions in the defect and non-defect region. Automatic inclusion analysis on a polished sample and inclusion observation on the cross-section of the defect zone were further

tested to elucidate the forming mechanism of the sliver defects on the automobile exposed plate.

2. Experimental

2.1. Sample characteristics

The defect on the surface of the cold-rolled alloyed hot-dip galvanized car's exposed panel was observed along the sheet's rolling direction, as shown in Fig. 1. The defect was about 1000 mm long, and 3 mm wide, irregularly distributed in the sheet's wide direction. The chemical composition of the automobile exposed panel is shown in Table 1. It is the conventional ultra-low carbon BH (bake hardening) steel that contains higher levels of Mn (about 0.65wt%), P (about 0.035wt%), and S (0.01wt%–0.015wt%) than the standard ultra-low carbon interstitial free (IF) steel.

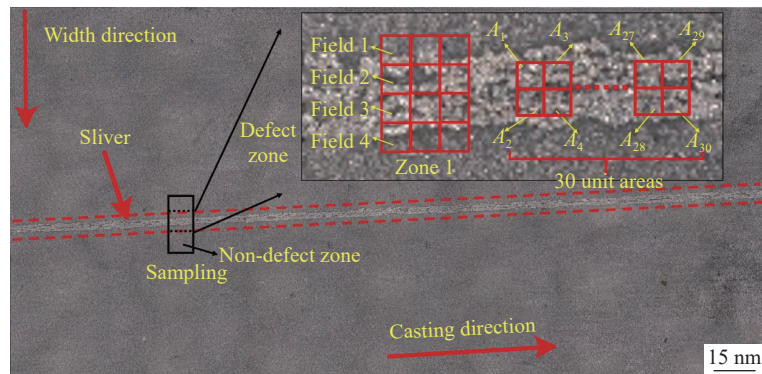


Fig. 1. Macro-morphology of sliver defect.

Table 1. Chemical composition of automobile exposed panel

	C	Si	Mn	P	S	Al	Nb	Ti	O	N	wt%
	0.0024	0.0070	0.6380	0.0365	0.0130	0.0446	0.0049	0.0045	0.0016	0.0017	

2.2. Quantitative electrolysis

Several 10 mm × 20 mm defect zone samples were cut out from the sheet. After 5 min of cleaning with an ultrasonic alcohol cleaner, in an electrolytic solution consisting of bromine methanol, deionized water, and 10vol% HCl with a volume ratio of 4:4:2, the samples were electrolyzed at the different selected times under room temperature. The device for electrolysis is shown in Fig. 2.

The inclusions have various morphologies because they may be found far from or near the surface in the steel sheet. Only the surface morphology can be studied without electrolysis rather than the three-dimensional morphology of inclusions. However, the three-dimensional morphology of inclusions at different locations can be studied using the quantitative electrolysis process, which is of great importance to explain the sliver defect formation mechanism. The zinc layer, as well as a small amount of steel sheet, was gradually removed by controlling the electrolytic time. The inclusions

near the steel sheet surface could be therefore exposed, demonstrating the three-dimensional morphology. Eqs. (1)–(4) determined the electrolyte time, according to the specific thickness of the zinc sheet. The current surface density was maintained at 0.01 A·mm⁻².

$$Q = I \cdot t \quad (1)$$

$$n_{\text{Fe}^{2+}} \text{ or } n_{\text{Zn}^{2+}} = \frac{Q}{2eN_A} = \frac{Q}{2 \times 1.6 \times 10^{-19} \times 6.02 \times 10^{23}} \quad (2)$$

$$h_{\text{Fe}} = \frac{M_{\text{Fe}} \cdot n_{\text{Fe}^{2+}}}{\rho_{\text{Fe}} \cdot S} \quad (3)$$

$$h_{\text{Zn}} = \frac{M_{\text{Zn}} \cdot n_{\text{Zn}^{2+}}}{\rho_{\text{Zn}} \cdot S} \quad (4)$$

where Q is the electric charge (C) quantity; I is the current (A); t is the time of erosion (s); $n_{\text{Fe}^{2+}}$ and $n_{\text{Zn}^{2+}}$ are the mole number of Fe²⁺ and Zn²⁺ (mol), respectively; N_A is the Avogadro constant (6.02×10^{23}); M_{Fe} and M_{Zn} are the molar mass of Fe and Zn ($\text{kg} \cdot \text{mol}^{-1}$), respectively; the area and

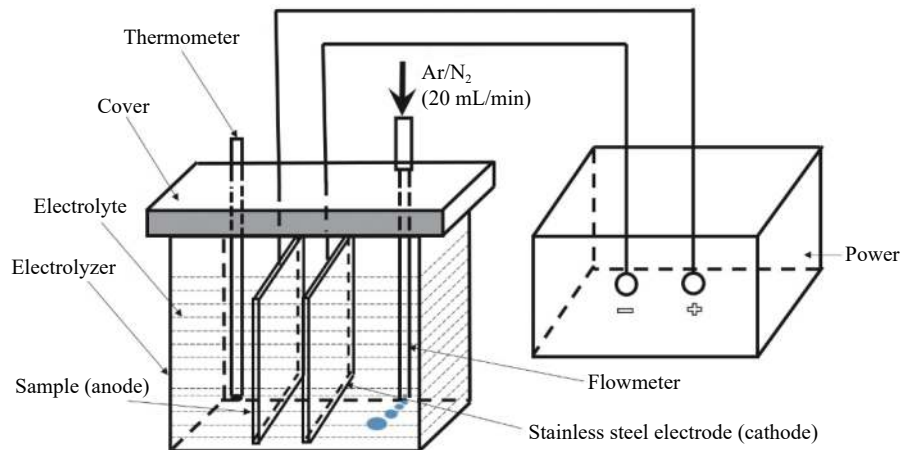


Fig. 2. Schematic diagram of electrolytic device.

thickness of erosion are S (m^2) and h (m), respectively; ρ_{Fe} and ρ_{Zn} are the density of steel and zinc ($kg \cdot m^{-3}$), respectively.

2.3. Observation and analysis of inclusion

The samples were cleaned with alcohol after electrolysis and then dried. The Carl Zeiss AG's EV018 SEM-EDS (scanning electron microscope-energy dispersive spectrometer) was used to analyze the three-dimensional morphology, composition, size, quantity, and distribution characteristics of inclusions in the defect and non-defect zone. Each defective sample contains fields 1–4 in the direction of width, as shown in Fig. 1. Inclusions of samples along the rolling direction were found from left to right. The area fractions of inclusions in the defect and non-defect region were measured by Image J software at 100 magnification for 30 unit areas in the defect region (A_1 – A_{30} as shown in Fig. 1). Each unit area was 1 mm^2 , and the total area of each sample was approximately 30 mm^2 in the defect or non-defect region. IAAS (Inclusions Automatic Analysis System) has analyzed the inclusions in the defect and non-defect region. IAAS consists of SEM-EDS and inclusion analysis software of Feature (Oxford Instruments, UK), which can automatically analyze inclusion morphology, composition, size, quantity, and distribution. Also analyzed were the inclusions in the cross-section of the defect. The cross-section of the defective sample was embedded in the mounting press, and the inlaid sample was polished to a smooth surface. The longitudinal morphology and thickness of zinc layer of the defect were observed by SEM, and EDS analyzed inclusions at the interface between the zinc layer and the steel sheet.

3. Results and discussion

3.1. Thermodynamic calculation

The evolution of inclusions during solidification were calculated by FactSage 7.3 based on the steel compositions

shown in Table 1. Ftoxicide (for oxides) and FSSStel (for molten steel) solution databases were employed in Factsage 7.3 Equilib module. The result is shown in Fig. 3. It can be seen that Al_2O_3 and MnS are the major inclusions in the steel. Because the MnS precipitation temperature is lower than that of the solidus line, it precipitates after the molten steel has been solidified. One part of pure MnS inclusions are very small in size [26–27], which ought not to be the main inclusions that cause the surface defect. The other part of MnS inclusions will precipitate on the core of Al_2O_3 forming complex inclusions of Al_2O_3 –MnS. The endogenous inclusions that influence the surface defect of the alloyed hot-dip galvanized sheet may, therefore, be Al_2O_3 inclusions or complex inclusions of Al_2O_3 –MnS.

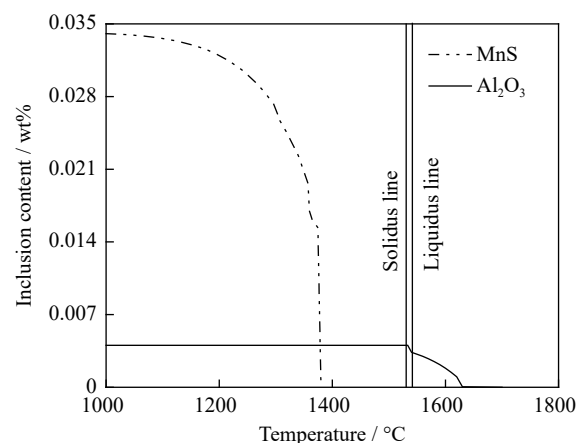


Fig. 3. Evolution of inclusions during solidification determined from the thermodynamic database.

3.2. Inclusions in the defect and non-defect zone after quantitative electrolysis

3.2.1. Determination of electrolytic conditions

Zinc-layered samples were electrolyzed for 5, 10, 15, 20, and 25 min under 0.1 A constant electrolytic current and

1 mm² electrolytic area. Fig. 4 is the defect zone morphologies with different electrolytic times. The zinc layer is blocked without electrolysis, as shown in Fig. 4(a). In Fig. 4(b), the zinc layer is partially removed with electrolysis for 5 min. When the electrolytic time increases to 10 min, the zinc layer is completely removed and the steel sheet is retained as shown in Fig. 4(c). From Fig. 4(d), it can be deduced that the

steel sheet starts to erode with electrolysis along the grain boundary for 15 min. The steel sheet is further eroded along the grain boundary after 20 min of electrolysis, as shown in Fig. 4(e). Fig. 4(f) indicates that most of the steel sheet's grain boundary is lost after 25 min of electrolysis. Therefore, with electrolysis for 5–20 min, the zinc layer can be removed in varying degrees, which is ideal for inclusion observation.

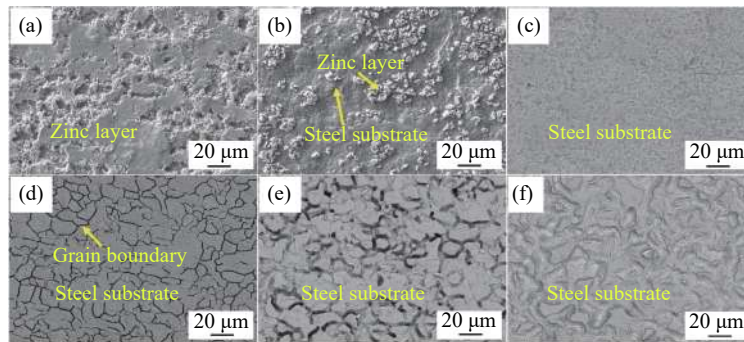


Fig. 4. Defect zone morphologies with specific electrolytic time: (a) non-electrolysis; (b) 5 min; (c) 10 min; (d) 15 min; (e) 20 min; (f) 25 min.

The inclusions gradually emerged from the surface at the various positions after conducting electrolysis at different times, and their three-dimensional morphology could be well observed. Analytical results of polished morphologies, three-dimensional morphologies, and energy spectrum for the inclusion in the defect zone are shown in Fig. 5. The observed inclusions can be identified to be predominantly Al₂O₃ with a size of 2–10 μm. As shown in Figs. 5(a)–5(c), they are blocky, rod-like, or irregular in shape in each case. The internal composition and size of inclusions on the polished portion are established by examining the polished morphology. While the actual size of the inclusions is more precise and re-

latively large, the external morphology is more practical by observing the three-dimensional morphology. The combined study of polished and three-dimensional morphologies can be used to understand the internal and external characteristics of inclusions comprehensively.

3.2.2. Inclusions of aggregation distribution in the defect zone after quantitative electrolysis

The defect in the samples was evaluated from left to right along the rolling direction, with quantitative electrolysis for 5–20 min. Interestingly, aggregated inclusions were observed in the defect zone. Parts of the inclusion aggregation were distributed discontinuously along the direction of rolling, with a spacing of 3–7 mm, a length of 6–7 mm, and a width of about 3 mm, covering the entire width of the defect. Fig. 6 shows the map scanning result of the distribution of the Al element in Zone 1 of the defect region as shown in Fig. 1, this corresponds to the Al₂O₃ distribution. The distribution of O element is not shown in-depth here since it is identical to Al distribution. The Al₂O₃ inclusion aggregation part can be found to cover the entire width of the defect.

The aggregated inclusions for 30 unit areas, A₁ to A₃₀, shown in Fig. 1 were also analyzed based on the above observation. It is indicated that 45 mm⁻² and 0.08%, respectively, are the average number density and area fraction of inclusions in the inclusion aggregation parts. The conventional morphologies of inclusion in the parts of the inclusion aggregation are obtained in Fig. 7. Such inclusions are granular, large, or irregular in shape, which are found on the surface of the steel sheet with size about 3–10 μm. The analysis of the energy spectrum reveals that these are Al₂O₃ inclusions, some of which contain a small amount of Mn and S. The elements

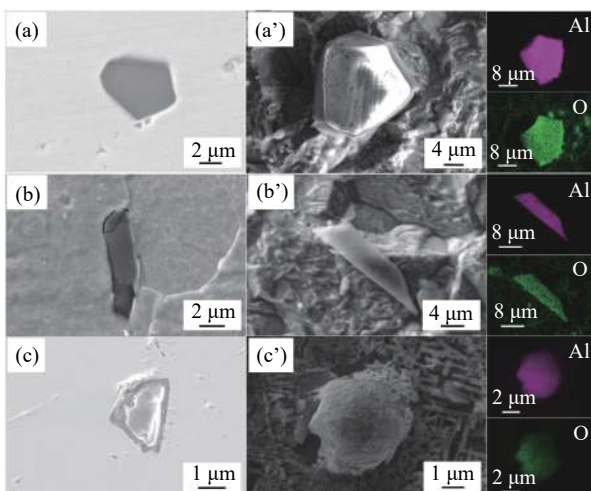


Fig. 5. Polished and three-dimensional morphology and energy spectrum analysis result of (a) blocky, (b) rodlike, and (c) irregular inclusions.

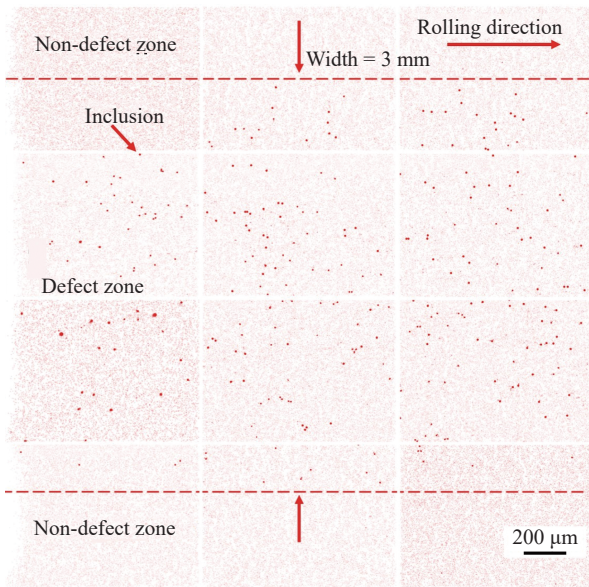


Fig. 6. Map scanning of the distribution of the Al element in the zone of defect and non-defect.

of Al, O, Mn, and S are normalized as listed in Table 2.

3.2.3. Inclusions of chain-like distribution in the defect zone after quantitative electrolysis

Besides, the chain-like inclusions distributed along the

rolling direction can also be observed between the inclusion aggregation parts in the defect zone where multiple inclusions are distributed discretely and discontinuously along the rolling direction with different distances of 10–150 μm. The length of each chain-like inclusion ranges from 200 to 800 μm. Fig. 8 shows the morphologies of the chain-like inclusion parts with different electrolysis times. The chain-like inclusion part shown in Fig. 8(d) is described as an example. The chain-like inclusion part is about 200 μm long, in which the inclusions are distributed with a spacing of 30–50 μm along the rolling direction. The map scanning result for the distribution of elements shows that these inclusions are mainly Al₂O₃ as the usual inclusions in the cold-rolled sheet. The specific inclusion morphologies 1–6 in Fig. 8(d) are shown in Figs. 8(e)–8(j), respectively. These inclusions are approximately 3–10 μm in size, circular or irregular in shape, with a rough surface, situated at the steel sheet’s grain boundary. The steel sheet started to erode along the grain boundary after the zinc layer is removed completely, then inclusions at the grain boundary slowly appeared. The average spacing of inclusions in 30 chain-like inclusion parts was calculated by the software of Image J as shown in Fig. 9. The inclusion spacing can be found to be primarily within the range of 40–160 μm, with an average value of 68.76 μm.

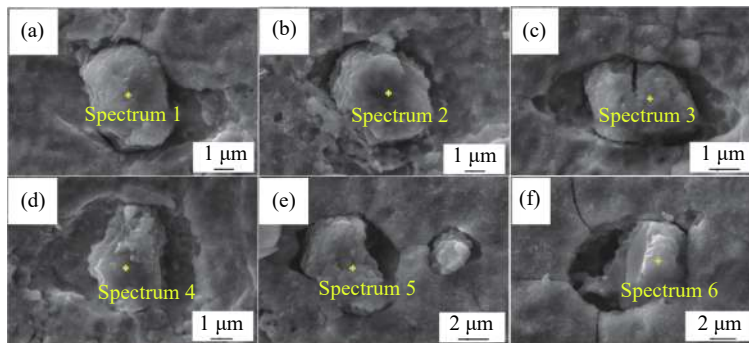


Fig. 7. Inclusions with (a–c) granular and (d–f) irregular shape in the inclusion aggregation parts.

3.2.4. Inclusions in the non-defect zone after quantitative electrolysis

Also analyzed were the inclusions in the non-defect zone following quantitative electrolysis. The result shows that in the non-defect zone where the number density of inclusions

is significantly reduced, there were no aggregated and chain-like inclusions. Fig. 10 exhibits the map scanning results of Al element distribution in the non-defect zone. At 100 magnification, there were only a few dispersed inclusions distributed in the non-defect zone. The standard inclusion morphologies in the non-defect region are shown in Fig. 11. Such inclusions are with granular or irregular shape and are situated near the steel sheet top. These inclusions are about 1–3 μm in size, which are smaller than the inclusions of the 3–10 μm in defect zone. These are Al₂O₃ inclusions containing a small number of elements of Mn and S. Table 3 illustrates the normalized contents of Al, O, Mn, and S. The Mn and S contents in the non-defect zone inclusions are higher than those in the defect zone, because the number of inclusions in the non-defect region is smaller and the same volume of MnS

Table 2. Compositions of inclusions in the aggregation parts of inclusions wt%

Inclusion	O	Al	S	Mn
1	47.30	49.92	0.90	1.88
2	48.07	51.93	0.00	0.00
3	52.22	42.74	1.26	3.78
4	49.09	48.02	0.72	2.17
5	50.00	50.00	0.00	0.00
6	48.65	51.35	0.00	0.00

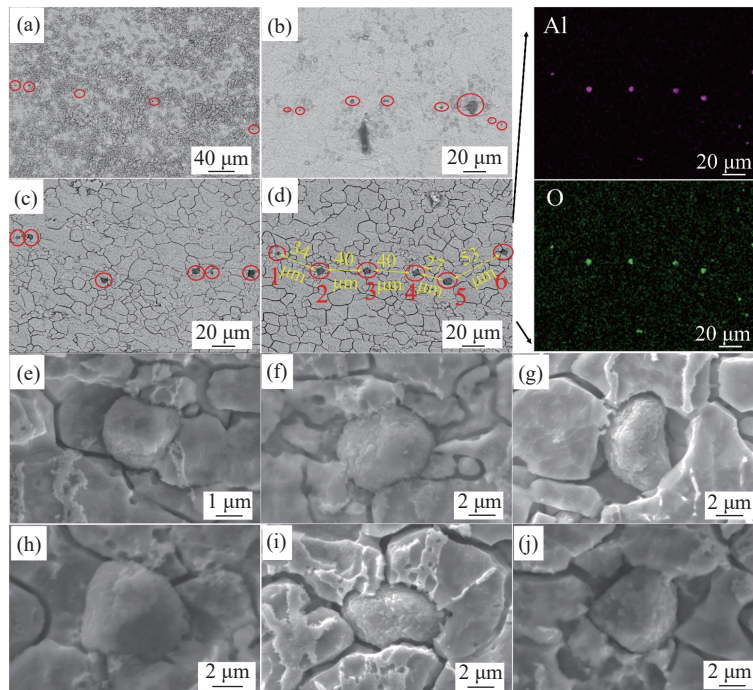


Fig. 8. Typical chain-like inclusion morphologies with different electrolytic time: (a) 5 min; (b) 10 min; (c) 15 min; (d) 20 min; (e–j) extended inclusion morphologies 1–6 in (d).

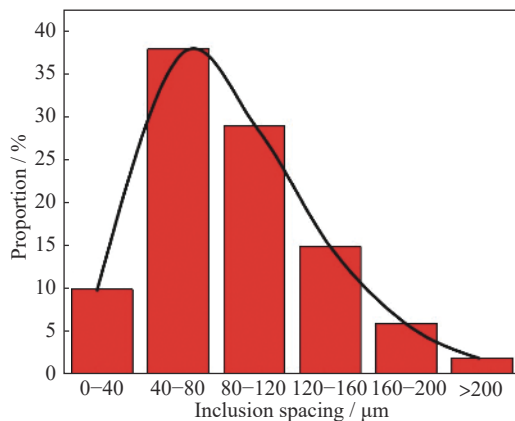


Fig. 9. Distribution of the inclusion spacing in the chain-like inclusion parts.

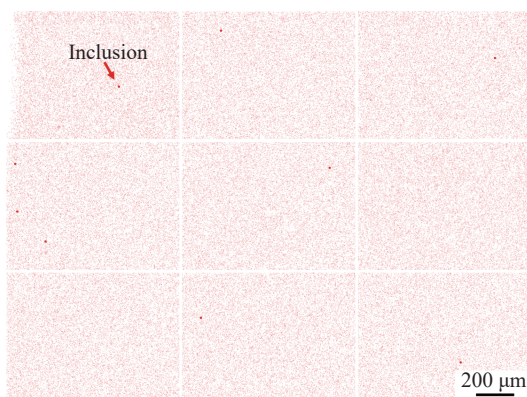


Fig. 10. Map scanning of the Al element distribution in the non-defect zone.

precipitation shares higher content on these smaller Al_2O_3 inclusions. Nevertheless, these small inclusions have little impact on the surface consistency of the slabs.

3.2.5. Comparison of inclusions in the defect and non-defect zone

The distributions of average inclusion area fraction for 30 unit areas in the defect zone of the inclusion aggregation parts and the non-defect zone are obtained in Fig. 12. The area fraction of inclusions in the inclusion aggregation parts is between 0.04%–0.16%, with an average value of 0.08%, which is higher than that in the non-defect zone with an average value of 0.0016%. In the non-defect zone, the number density of inclusions is 1–2 mm^{-2} , which is much less than that in the defect zone of 40 mm^{-2} .

To calculate and compare the inclusion spacing in the non-defect zone and the defect zone of the aggregated and chain-like inclusion parts easily, the inclusion spacing, L (μm), is estimated according to the following equation:

$$L = \sqrt{\frac{4}{N \cdot \pi}} \tag{5}$$

where N is the inclusion number per unit area (μm^{-2}). Eq. (5) is interpreted as being capable of corresponding to an equal circle of the sample with an area of $\frac{1}{N}$, and the radius of the circle is half the distance between two inclusions. Then Eq. (5) is deduced from the following formula:

$$\frac{1}{N} = \pi \left(\frac{L}{2}\right)^2 \tag{6}$$

Fig. 13 shows the average inclusion size distributions in

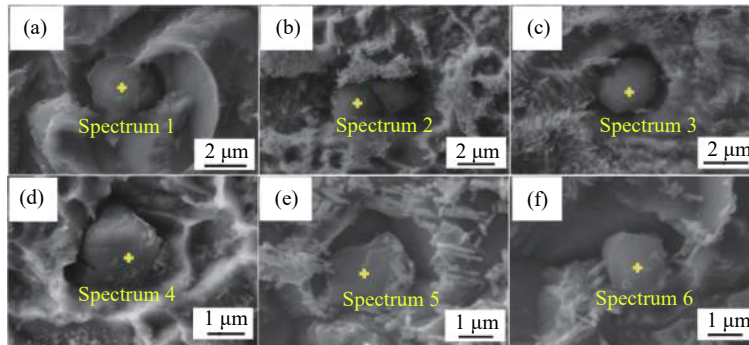


Fig. 11. Inclusions with (a–c) granular and (d–f) irregular shape in the non-defect zone.

Table 3. Compositions of inclusions in the non-defect zone

Inclusion	O	Al	S	Mn
1	39.82	54.49	2.13	3.56
2	39.32	50.17	3.75	6.76
3	40.12	51.43	3.13	5.32
4	40.61	48.33	3.69	7.37
5	43.03	49.91	2.45	4.61
6	31.83	53.97	4.74	9.46

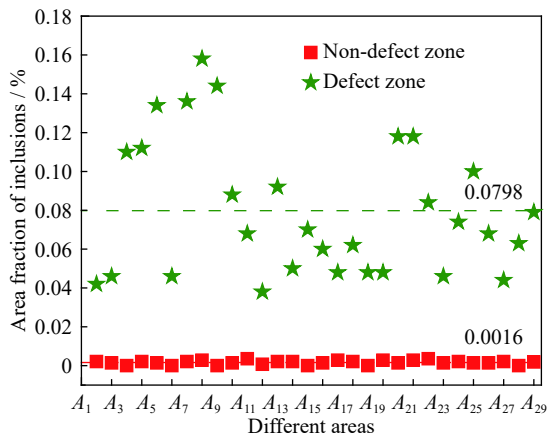


Fig. 12. Area fraction of inclusions for the non-defect and defect zone in the various areas.

the above three areas for 30 unit areas. The inclusion spacing of the aggregated and chain-like inclusion parts in the defect zone is less than 100 μm, with an average of 25.13 and 68.66 μm respectively. Nevertheless, the value in the non-defect is about 402.66 μm, except for some non-inclusive regions. So, it is believed that the inclusion spacing in the defect zone is significantly smaller than that in the non-defect zone.

However, inclusions with a size smaller than 1 μm by SEM–EDS at 100 magnification after electrolysis are difficult to be observed. Therefore, the IAAS was used for automatic inclusion statistics for 40 mm² in the defect and non-defect zone to compare the small inclusions between the zones. IAAS identified the proportions of inclusions with varying sizes in the defect and non-defect zone as shown in Fig. 14. The proportion of inclusions with a size of less than

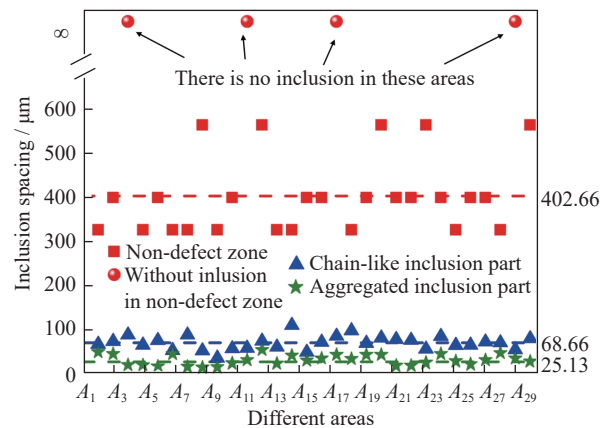


Fig. 13. Inclusion spacing in the non-defect zone and defect zone containing chain-like inclusion parts and the aggregated inclusion parts.

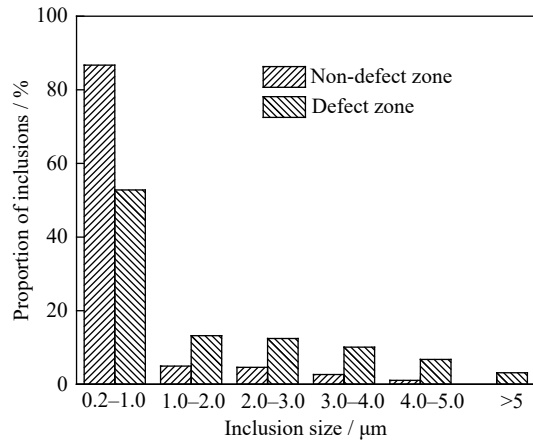


Fig. 14. IAAS analysis result of inclusions in the defect and non-defect zone.

1 μm in the non-defect zone is higher than that in the defect zone. The average inclusion sizes greater than 1 and 0.2 μm in the defect zone are 4.45 and 1.61 μm, respectively, larger than 3.20 and 1.12 μm in the non-defect zone. The normalized IAAS inclusion contents of O, Al, S, and Mn in the defect and the non-defect zone are shown in Fig. 15. The contents of S and Mn for inclusions in the defect zone are lower

than those in the non-defect zone by IAAS. The results of IAAS obtained as discussed above are identical to the results of quantitative electrolysis. It is concluded that the inclusions in the defect zone are mostly pure, large-sized Al_2O_3 inclusions, which are secondary oxidation products containing less MnS. However, the inclusions in the non-defect zone are mostly small-sized Al_2O_3 inclusions, which are deoxidation products that contain more MnS. During solidification, MnS is easy to precipitate around these small inclusions and form the complex Al_2O_3 -MnS inclusions, so that the contents of Mn and S for inclusions in the non-defect zone are higher than those in the defect zone.

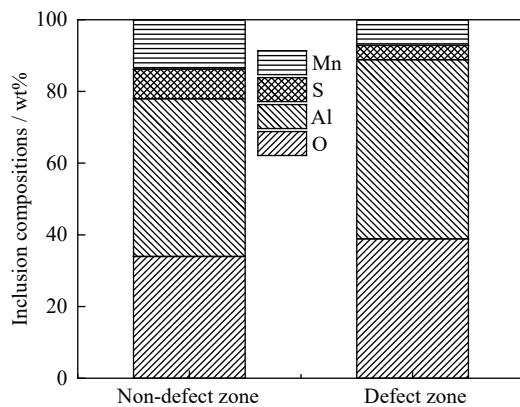


Fig. 15. Normalized compositions of the inclusions in the defect and non-defect zone.

3.3. Inclusions on cross-section of the defect zone

Inclusions on the cross-section of samples were also stud-

ied after the above analysis of inclusions on the sample surface. The defect zone cross-section was observed as shown in Fig. 16. With a thickness of 7–10 μm , the zinc layer is slightly fragmented. Besides, at the interface between the zinc layer and the steel surface, granular and stripped inclusions were observed as shown in Fig. 16(a). The findings of Al_2O_3 inclusions are indicated by the energy spectrum analysis in Figs. 16(b)–16(c). The zinc layer and steel sheet are delaminated by the Al_2O_3 inclusions, leading to some gaps in the zinc layer. The Al_2O_3 inclusions on the defect zone cross-section are the same as the Al_2O_3 in the aggregated and chain-like inclusion parts on the defect zone surface.

3.4. Formation mechanism of sliver defect

There are few previous studies on the detail distribution characteristics of inclusions in the defects. The results and analysis described above can provide the basis for the defect formation mechanism discussed as follows. The schematic diagram of the sliver defect formation mechanism on the alloyed hot-dip galvanized automobile exposed panel surface is described in Fig. 17, which involves the rolling cycle of the defect, and the top and cross-section views of the defect are shown in Fig. 17(a) and Figs. 17(b) and 17(c) in each case.

There are aggregated and chain-like Al_2O_3 inclusion parts along the rolling direction in the defect zone as revealed in Fig. 17(b). In the defect area, the area fraction, number density, and size of Al_2O_3 are greater than those in the non-defect zone. As Fig. 17(c) describes, Al_2O_3 inclusions are also present on the cross-section of the defect region, including only the inclusions near the steel sheet surface as shown in

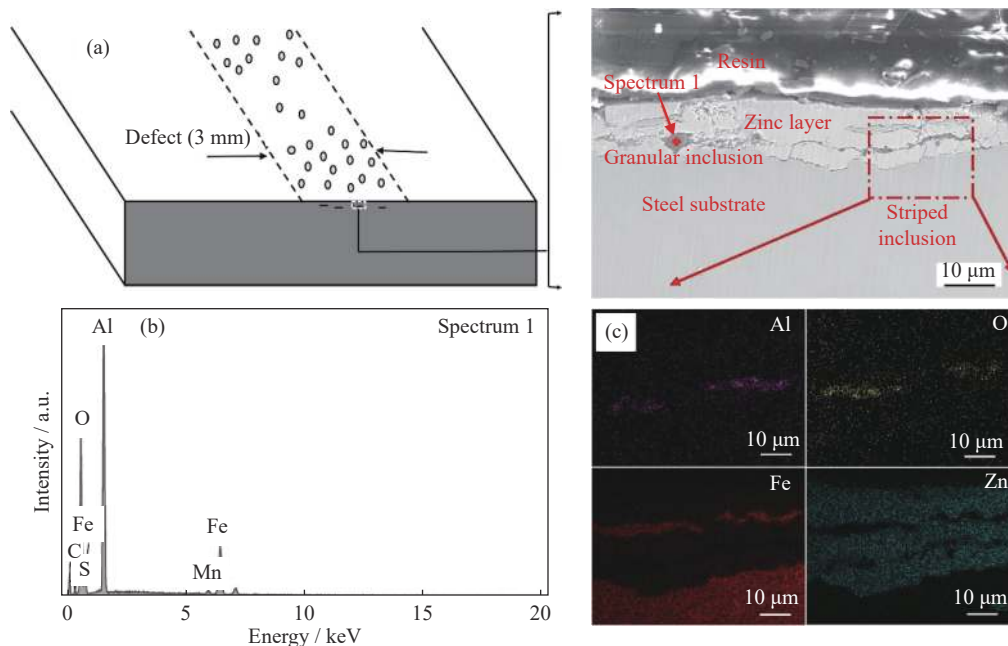


Fig. 16. Schematic diagram (a), EDX point analysis (b), and (c) element map scanning analysis of observed morphology of inclusions in the cross-section of the defect zone.

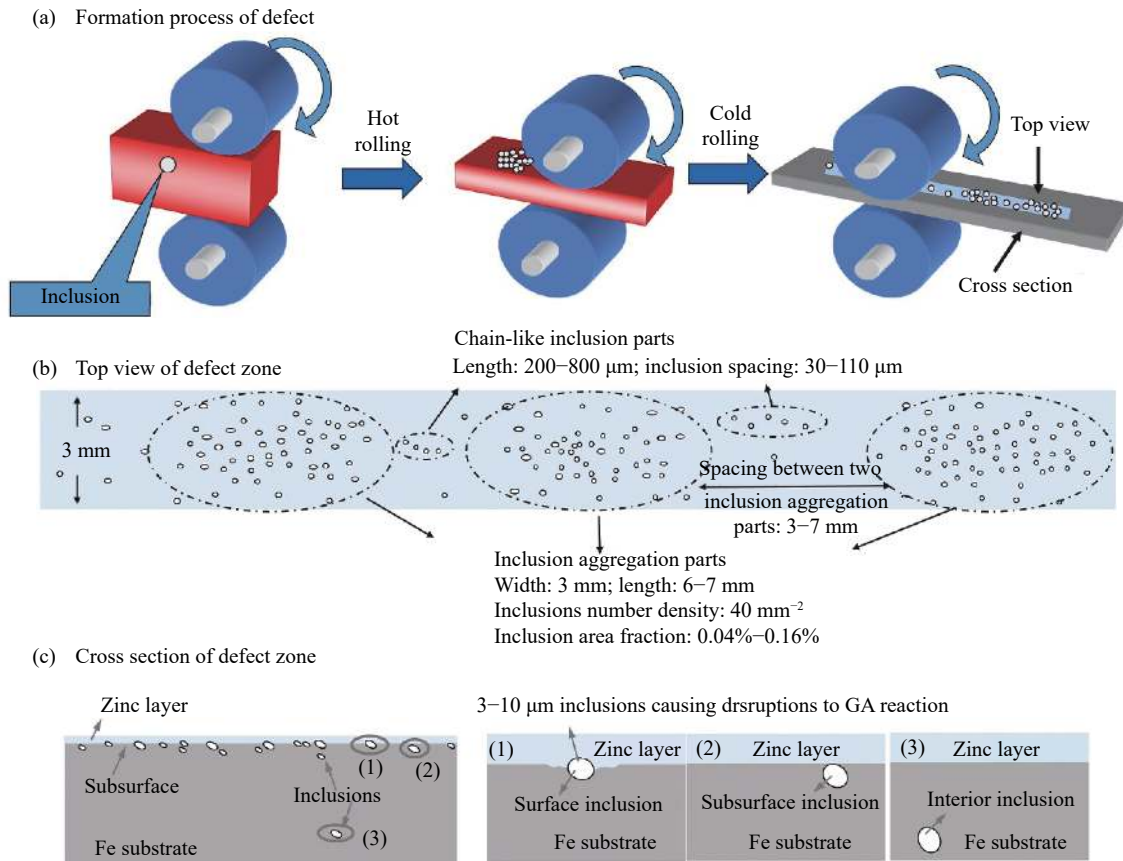


Fig. 17. Schematic diagram of the defect on the automobile exposed panel surface: (a) the formation process, (b) the top view, and (c) the cross section.

Fig. 17(c) are responsible for the surface defect. The Al_2O_3 inclusions in the defect zone are predominantly large, which may result from secondary oxidation products or clogging of the nozzle. Most of them are granular, large, or irregular in form without apparent elongation. It's because these inclusions are brittle and non-deformable inclusions with a high melting point and low ductility.

After the rolling process, large-size Al_2O_3 inclusions like in clustered form near the slab surface are completely crushed, then discretely dispersed along the rolling direction and slowly revealed in aggregated or chain-like shape. The steel surface will be scratched and these inclusions will reduce the deformability with high stiffness. The steel sheet integrity is lost, resulting in accumulation of stress and poor bonding between the substrate and the inclusions. Accordingly, the surface defect is finally formed when the sheet is rolled to a certain thickness. In addition, during the process of alloying and hot-dip galvanizing, these inclusions can easily interfere with the galvanizing and alloying (GA) reaction, alter the relative proportions of the various Fe–Zn intermetallic phases, and result in a deviation from the usual matt surface of the alloyed hot-dip galvanized strip. Consequently, the sliver defect is more obvious after alloying and hot-dip galvanizing [18,28]. The harmfulness increases as the inclusion

size increases. The frequency of large Al_2O_3 inclusions near the surface of the IF steel slab (such as within 1/8 of the slab surface or within 3.5 mm of the slab surface) should be strictly controlled and the critical size of the harmful inclusions is approximately 100 μm [1–2,7,14]. Therefore, the main countermeasure for controlling surface defects from Al_2O_3 inclusions is to decrease the large-size Al_2O_3 inclusions near the slab surface.

4. Conclusions

The sliver defect on the cold-rolled alloyed hot-dip galvanized automobile exposed panel was studied to reveal the specific distribution characteristics of inclusions along with the sliver defect and to clarify its formation mechanism. The findings are as follows.

(1) It was discovered that using the quantitative electrolysis method, an aggregated or chain-like inclusion pieces were dispersed in the defect containing Al_2O_3 inclusions formed in the steelmaking process, which were crushed and exposed during the rolling process, resulting in the sliver defect on the cold-rolled surface.

(2) The Al_2O_3 inclusion aggregation parts were distributed discretely in the defect zone along the rolling direction

with a spacing of 3–7 mm, a length of 6–7 mm, and a width of approximately 3 mm. The size of Al_2O_3 is mainly 3–10 μm . The inclusion area fraction is 0.04%–0.16% with an average value of 0.08%, the number density of inclusions is 40 mm^{-2} and the average inclusion spacing is 25.13 μm .

(3) In the defect zone, the inclusion spacing in the chain-like inclusion parts is largely 40–160 μm with an average value of 68.76 μm . Al_2O_3 is also primarily 3–10 μm in size.

(4) The number density and the size of inclusions in the non-defect zone decreases substantially compared to those in the defect zone. The average inclusion area fraction, inclusion number density, and inclusion spacing is approximately 0.002%, 1–2 mm^{-2} , and 400 μm , respectively, with an Al_2O_3 size of 1–3 μm .

Acknowledgements

This work was financially supported by the National Natural Science Foundation of China (No. U1960202).

References

- [1] M. Wang and Y.P. Bao, Source and negative effects of macro-inclusions in titanium stabilized ultra low carbon interstitial free (Ti-IF) steel, *Met. Mater. Int.*, 18(2012), No. 1, p. 29.
- [2] Q.Y. Zhang, L.T. Wang, and X.H. Wang, Influence of casting speed variation during unsteady continuous casting on non-metallic inclusions in IF steel slabs, *ISIJ Int.*, 46(2006), No. 10, p. 1421.
- [3] H. Esaka, Y. Kuroda, K. Shinozuka, and M. Tamura, Interaction between argon gas bubbles and solidified shell, *ISIJ Int.*, 44(2004), No. 4, p. 682.
- [4] H. Yasunaka, R. Yamanka, T. Inoue, and T. Saito, Pinhole and inclusion defects formed at the subsurface in ultra low carbon steel, *Tetsu-to-Hagané*, 81(1995), No. 5, p. 529.
- [5] X.X. Deng, L.P. Li, X.H. Wang, Y.Q. Ji, C.X. Ji, and G.S. Zhu, Subsurface macro-inclusions and solidified hook character in aluminum-killed deep-drawing steel slabs, *Int. J. Miner. Metall. Mater.*, 21(2014), No. 6, p. 531.
- [6] H. Yamamura, Y. Mizukami, and K. Misawa, Formation of a solidified hook-like structure at the subsurface in ultra low carbon steel, *ISIJ Int.*, 36(1996), No. Suppl, p. S223.
- [7] X.X. Deng, C.X. Ji, Y. Cui, Z.H. Tian, X. Yin, X.J. Shao, Y.D. Yang, and A. McLean, Formation and evolution of macro inclusions in IF steels during continuous casting, *Ironmaking Steelmaking*, 44(2017), No. 10, p. 739.
- [8] J. Sengupta, B.G. Thomas, H.J. Shin, G.G. Lee, and S.H. Kim, A new mechanism of hook formation during continuous casting of ultra-low-carbon steel slabs, *Metall. Mater. Trans. A*, 37(2006), No. 5, p. 1597.
- [9] G.G. Lee, H.J. Shin, S.H. Kim, S.K. Kim, W.Y. Choi, and B.G. Thomas, Prediction and control of subsurface hooks in continuous cast ultra-low-carbon steel slabs, *Ironmaking Steelmaking*, 36(2009), No. 1, p. 39.
- [10] M. Zeze, A. Tanaka, and R. Tsujino, Formation mechanism of sliver-type surface defect with oxide scale on sheet and coil, *Tetsu-to-Hagané*, 87(2001), No. 2, p. 85.
- [11] T. Miyake, M. Morishita, H. Nakata, and M. Kokita, Influence of sulphur content and molten steel flow on entrapment of bubbles to solid/liquid interface, *ISIJ Int.*, 46(2006), No. 12, p. 1817.
- [12] H.X. Yu, C.X. Ji, B. Chen, C. Wang, and Y.H. Zhang, Characteristics and evolution of inclusion induced surface defects of cold rolled IF sheet, *J. Iron Steel Res. Int.*, 22(2015), No. Supplement 1, p. 17.
- [13] S. Das, S. Roy, S. Nayak, T. Bhattacharyya, and S. Bhattacharyya, Case study—Analysis of grayish stick type sliver in cold rolled strips, *Eng. Fail. Anal.*, 44(2014), p. 95.
- [14] H. Cui, H.J. Wu, F. Yue, W.S. Wu, M. Wang, Y.P. Bao, B. Chen, and C.X. Ji, Surface defects of cold-rolled Ti-IF steel sheets due to non-metallic inclusions, *J. Iron Steel Res. Int.*, 18(2011), Suppl. 2, p. 335.
- [15] C. Genzano, J. Madias, D. Dalmaso, J. Petroni, D. Biurrun, and G.D. Gresia, Elimination of surface defects in cold-rolled extra low carbon steel sheet, [in] *the ISS 85th Steelmaking Conference*, Nashville, 2002, p. 325.
- [16] P. Záhumný and M. Merwin, Evolution of artificial defects from slab to rolled products, *J. Mater. Process. Technol.*, 196(2008), No. 1-3, p. 266.
- [17] H. Utsunomiya, K. Hara, R. Matsumoto, and A. Azushima, Formation mechanism of surface scale defects in hot rolling process, *CIRP Ann.*, 63(2014), No. 1, p. 261.
- [18] S. Moir and J. Preston, Surface defects—evolution and behaviour from cast slab to coated strip, *J. Mater. Process. Technol.*, 125-126(2002), p. 720.
- [19] R. Inoue, K. Kiyokawa, K. Tomoda, S. Ueda, and T. Ariyama, Three dimensional estimation of multi-component inclusion particle in steel, *Metall. Anal.*, 32(2012), No. 8, p. 1.
- [20] D. Janis, R. Inoue, A. Karasev, and P.G. Jönsson, Application of different extraction methods for investigation of nonmetallic inclusions and clusters in steels and alloys, *Adv. Mater. Sci. Eng.*, 2014(2014), art. No. 210486.
- [21] Y.P. Bao, M. Wang, and W. Jiang, A method for observing the three-dimensional morphologies of inclusions in steel, *Int. J. Miner. Metall. Mater.*, 19(2012), No. 2, p. 111.
- [22] X.W. Zhang, L.F. Zhang, W. Yang, Y. Wang, Y. Liu, and Y.C. Dong, Characterization of the three-dimensional morphology and formation mechanism of inclusions in linepipe steels, *Metall. Mater. Trans. B*, 48(2017), No. 1, p. 701.
- [23] J. Guo, S.S. Cheng, H.J. Guo, and Y.G. Mei, Determination of non-metallic inclusions in a continuous casting slab of ultra-low carbon interstitial free steel by applying of metallographic method, electrolytic method and RTO technique, *Sci. Rep.*, 9(2019), art. No. 2929.
- [24] R. Inoue, S. Ueda, T. Ariyama, and H. Suito, Extraction of non-metallic inclusion particles containing MgO from steel, *ISIJ Int.*, 51(2011), No. 12, p. 2050.
- [25] R. Inoue, R. Kimura, S. Ueda, and H. Suito, Applicability of nonaqueous electrolytes for electrolytic extraction of inclusion particles containing Zr, Ti, and Ce, *ISIJ Int.*, 53(2013), No. 11, p. 1906.
- [26] R. Diederichs and W. Bleck, Modelling of manganese sulphide formation during solidification, part I: Description of MnS formation parameters, *Steel Res. Int.*, 77(2006), No. 3, p. 202.
- [27] R. Diederichs, R. Bülte, G. Parisser, and W. Bleck, Modelling of manganese sulphide formation during solidification, Part II: Correlation of solidification and MnS formation, *Steel Res. Int.*, 77(2006), No. 4, p. 256.
- [28] Q.C. Peng, J.L. Yang, S. Peng, X.H. Zhang, S.P. Tang, and Y.S. Tian, Analysis of linear defects of cold-rolled galvanized sheet, *Adv. Mater. Res.*, 652-654(2013), p. 2034.